remote sensing

MDPI

Article

A Mars Local Terrain Matching Method Based on 3D Point Clouds

Binliang Wang [1,2], Shuangming Zhao [1,*], Xinyi Guo [3,4,5] and Guorong Yu [6]

[1] School of Remote Sensing and Information Engineering, Wuhan University, Wuhan 430079, China; blwang@whu.edu.cn
[2] State Key Lab of Information Engineering in Surveying, Mapping, and Remote Sensing (LIESMARS), Wuhan University, Wuhan 430079, China
[3] Beijing Institute of Surveying and Mapping, Beijing 100038, China; guoxinyi7@foxmail.com
[4] Beijing Key Laboratory of Urban Spatial Information Engineering, Beijing 100038, China
[5] Beijing Satellite Application Technology Center, Beijing 100038, China
[6] School of Computer Science and Technology, Wuhan University of Science and Technology, Wuhan 430081, China; yuguorong190@wust.edu.cn
* Correspondence: smzhao@whu.edu.cn

Abstract: To address the matching challenge between the High Resolution Imaging Science Experiment (HiRISE) Digital Elevation Model (DEM) and the Mars Orbiter Laser Altimeter (MOLA) DEM, we propose a terrain matching framework based on the combination of point cloud coarse alignment and fine alignment methods. Firstly, we achieved global coarse localization of the HiRISE DEM through nearest neighbor matching of key Intrinsic Shape Signatures (ISS) points in the Fast Point Feature Histograms (FPFH) feature space. We introduced a graph matching strategy to mitigate gross errors in feature matching, employing a numerical method of non-cooperative game theory to solve the extremal optimization problem under Karush–Kuhn–Tucker (KKT) conditions. Secondly, to handle the substantial resolution disparities between the MOLA DEM and HiRISE DEM, we devised a smoothing weighting method tailored to enhance the Voxelized Generalized Iterative Closest Point (VGICP) approach for fine terrain registration. This involves leveraging the Euclidean distance between distributions to effectively weight loss and covariance, thereby reducing the results' sensitivity to voxel radius selection. Our experiments show that the proposed algorithm improves the accuracy of terrain registration on the proposed Curiosity landing area's, Mawrth Vallis, data by nearly 20%, with faster convergence and better algorithm robustness.

Keywords: MOLA; HiRISE; point cloud registration; FPFH; graph matching

Citation: Wang, B.; Zhao, S.; Guo, X.; Yu, G. A Mars Local Terrain Matching Method Based on 3D Point Clouds. *Remote Sens.* **2024**, *16*, 1620. https://doi.org/10.3390/rs16091620

Academic Editor: Giancarlo Bellucci

Received: 21 March 2024
Revised: 21 April 2024
Accepted: 29 April 2024
Published: 30 April 2024

1. Introduction

Since 1975, humans have conducted numerous Mars exploration missions [1], yielding a wealth of images and topographic data. The key challenge in Mars mapping using multi-sensor and multi-source data lies in addressing the spatial reference data issue. In deep space photogrammetry, systematic errors in satellite orbital position parameters, typically stemming from planetary orbiter clock errors, star sensor measurement errors, and the Doppler effect, often range from hundreds to thousands of meters. Moreover, due to the low accuracy of satellite attitude orbit measurement data and the absence of control points on the planetary surface, Mars surface models reconstructed directly from satellite images frequently exhibit significant absolute offsets [2]. Previous studies [3–7] have demonstrated that Mars Orbiter Laser Altimeter (MOLA) [8,9] data can aid in the geometric positioning of Mars photogrammetry. The MOLA Digital Elevation Model (DEM) serves as an excellent global control reference for determining orbit and attitude parameters in Mars exploration missions and mapping endeavors [10]. By employing the MOLA DEM's results as the reference data, a large number of matching approaches were widely developed to further align the topography information from images and point cloud.

Topographic matching studies can be broadly categorized into two groups: image-based approaches and point cloud-based approaches. The image-based method involves rasterizing the 3D model and encoding elevation information into image grayscale, followed by employing image matching techniques for terrain alignment [11,12]. On the other hand, the point cloud-based method involves sampling terrain data into discrete point clouds and achieving terrain matching through registration between these point clouds. Point cloud registration is commonly implemented and further improved based on geometric feature descriptors matching or local distribution-based point-to-point alignment [13]. Feature-based methods are primarily utilized for coarse registration. Classic feature extraction algorithms for point clouds include Harris3D [14], SIFT 3D [15], Local Surface Patches (LSP) [16], MeshDoG [17], and Intrinsic Shape Signatures (ISS) [18], among others. Point cloud feature description methods include SHOT (Signature of Histograms of Orientations) [19], PFH (Point Feature Histogram) [20], FPFH (Fast Point Feature Histogram) [21], 3DSmoothNet [22], and more. On the other hand, the point-based approach achieves fine registration by establishing correspondence between the points in point clouds. Typical DEM fine registration methods include Least Z-difference (LZD) [23] and Iterative Closest Point (ICP) [24], both of which are constructed based on the least squares principle and require an initial pose estimation. As important as images, point cloud information [1,25] has been widely used for Martian topography descriptions in recent years. To provide accurate topographic maps of Mars (i.e., no distortion), it is important to develop matching approaches that use a point cloud.

The High Resolution Imaging Science Experiment (HiRISE) is a high-resolution imaging instrument carried by the Mars Reconnaissance Orbiter (MRO), capable of capturing ultra-high-resolution images of the Martian surface with a resolution of 0.25 m. It currently stands as the highest resolution camera for Mars exploration. The HiRISE has been proven to be highly effective in conducting local sub-meter terrain reconstruction and exploring geomorphology on Mars [2,10], playing a crucial role in studying the landing sites of missions such as Spirit [26] and Curiosity [27]. For precise positioning, the attitude orbit of HiRISE data should be calibrated by MOLA orbit data [28]. The DEM registration allows for the alignment of orbit data, combining HiRISE's high-resolution capabilities with MOLA's extensive coverage. This integration enables detailed analysis of Martian surface features, essential for geological studies, navigation, and planning. The process also aligns discrepancies in coordinate systems, ensuring accurate data comparison and analysis.

To achieve the absolute orientation of HiRISE data, our studies and contributions in this paper can be summarized as follows:

(1) DEM coarse registration. A DEM coarse registration framework based on the combination of ISS + FPFH features is proposed, and the feature matching gross errors are removed based on a graph strategy.
(2) DEM fine registration. For the problem of large difference in resolution between MOLA DEM and HiRISE DEM raw observation data, the loss and covariance are weighted by the Euclidean distance between distributions, and a smoothing weighting method is constructed to take into account the specificity and improve the VGICP fine registration algorithm.
(3) Experiment and analysis. To validate the proposed method, we apply it to real experimental data from Mars. The results demonstrate the effectiveness of our approach in solving the local terrain registration problem on Mars.

The algorithm flow chart of this paper is shown in Figure 1:

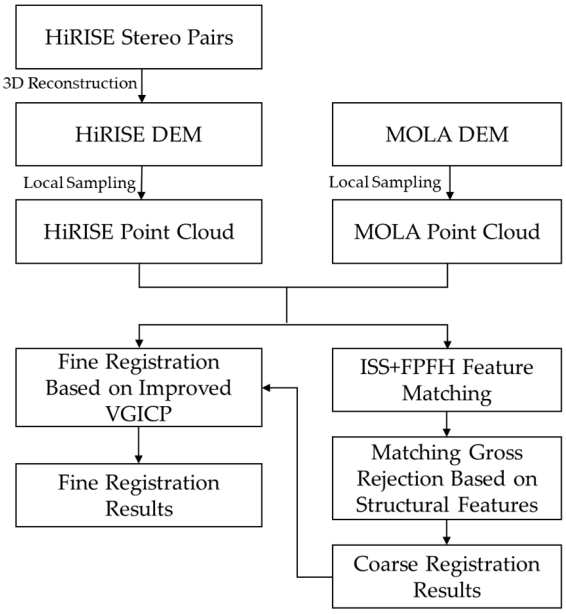

Figure 1. Framework for terrain registration method based on 3D point cloud.

2. DEM Coarse Registration Based on 3D Features

The MOLA DEM [29] was released by the Planetary Data System (PDS), and can be obtained from the United States Geological Survey (USGS) with a resolution of 463 m/pixel, while the resolution of the HiRISE image can be as fine as 0.25 m/pixel. In this paper, a uniform 64 × 64 pixel grid is used for stereo reconstruction, and its resolution can still reach 16 m or so. In order to maintain the advantages of high-resolution terrain data and standardize the algorithm input, we first up-sampled the 463 m/pixel MOLA DEM at 30 m resolution to match the order of magnitude of the HiRISE DEM point cloud. Meanwhile, the repeatability and identifiability of ISS feature points are better than other 3D key point detection algorithms [18,30], and the FPFH can achieve fast and robust feature description and matching tasks [21], so we choose to achieve coarse registration through the combination of ISS + FPFH features. The DEM coarse registration algorithm contains the following steps: (1) Extracting 3D key points using the ISS algorithm. (2) Calculating FPFH local feature descriptors based on the key point neighborhood and feature space nearest neighbor search to obtain the initial matched point pairs. (3) The initial point pairs usually contain a large number of mismatched point pairs due to local feature similarity or insignificant specificity of key points. In this paper, we introduce a graph matching strategy to eliminate the mismatches of the initial point pairs.

2.1. ISS Key Points and PFH/FPFH Features

Similar to image key point detection, the ISS algorithm [18] expresses the degree of point specificity by investigating the relationship between a sample point and a set of 3D points in its neighborhood. Before the coarse terrain registration, we first extract ISS key points from the point cloud to prepare for subsequent feature description and matching.

By statistically analyzing the spatial relationship between key points and their neighboring points, the Point Feature Histogram (PFH) can be established [20]. This histogram captures the geometric properties in the vicinity of the feature points. The high-dimensional histogram space offers a measurable information space that remains invariant to three-dimensional rotation and translation of the point cloud, and it exhibits a robustness against variations in sampling density and noise. As shown in Figure 2a, the key point p_q (red) is taken as the center, and k nearest neighbor p_{k_i} (blue) is searched for in the neighborhood of radius r. The $k+1$ points are paired two by two to generate $k(k+1)/2$ point pairs. The geometric features of all of the point pairs are calculated, and then the PFH feature descriptor of p_q can be obtained statistically. The specific algorithm is as follows:

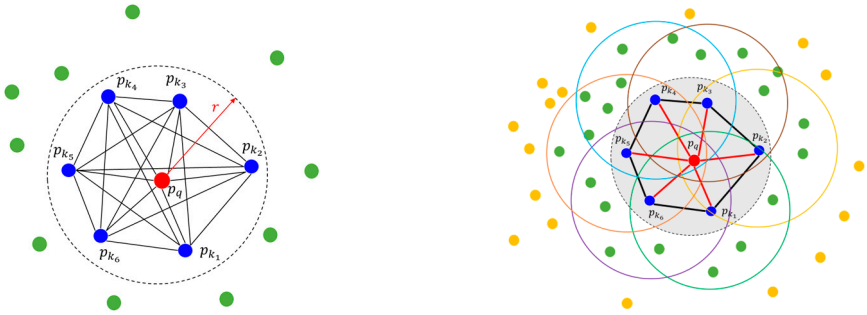

Figure 2. Point cloud feature calculation neighborhood. (**a**) PFH descriptor; (**b**) FPFH descriptor.

(1) Given the point pair $\{p_s, p_t\}$, a local coordinate system $p_s - \mu\nu\omega$ is established with p_s as the origin, corresponding to the direction of the coordinate axes as

$$\mu = n_s,\ \nu = \mu \times \frac{p_t - p_s}{\|p_t - p_s\|_2},\ \omega = \mu \times \nu \tag{1}$$

where $\times$ denotes the vector outer product and $\|p_t - p_s\|_2$ is the point-to-point Euclidean distance.

(2) Based on the local coordinate system, the point pair features can be represented by the $< \alpha, \phi, \theta, d >$ quadruple notation

$$\begin{aligned} \alpha &= \nu \cdot n_s \\ \phi &= \mu \cdot \frac{p_t - p_s}{d} \\ \theta &= \arctan(\omega \cdot n_t, \mu \cdot n_t) \\ d &= \|p_t - p_s\|_2 \end{aligned} \tag{2}$$

where $\cdot$ denotes the vector inner product, $\alpha,\ \phi,\ \theta$ are the angular features, d is the Euclidean distance, and $n_s,\ n_t$ are the normal vectors at $p_s,\ p_t$.

(3) The feature quadruplets $< \alpha, \phi, \theta, d >$ of each point pair in the neighborhood of key point p_q are calculated, and each dimensional feature is divided into n intervals. The number of interval votes is counted to obtain the histogram, and the feature vector with dimension n^4 is generated as the FPH feature descriptor of p_q (as shown in Figure 3).

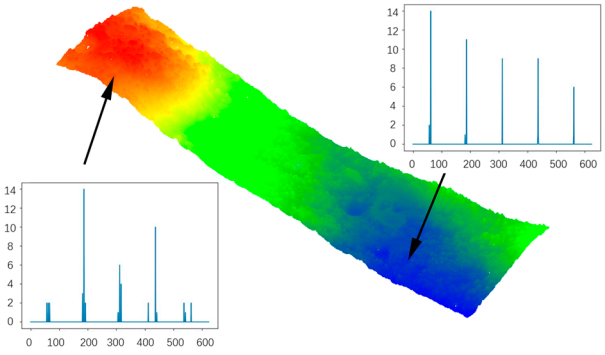

Figure 3. Example of PFH features histogram ($n = 5$).

The time complexity of PFH features is $O\left(nk^2\right)$, which is computationally inefficient. Rosu et al. proposed the FPFH algorithm [19], which reduces the time complexity to $O(nk)$ while preserving the feature description performance. The algorithm is improved as follows:

(1) When calculating the point pair features, only the angular components $< \alpha, \phi, \theta >$ are retained.

(2) The triplets of $< \alpha, \phi, \theta >$ are processed separately, and the histogram corresponding to each dimensional feature is simply stitched, so that the dimensionality of the synthetic features is reduced from n^3 to $3n$, effectively eliminating the spatial redundancy in the feature description process.

(3) Only the $< \alpha, \phi, \theta >$ features corresponding to the point pairs $\{p_q, p_{k_i}\}$ formed by the points p_q and the k nearest neighbors are calculated (as shown in Figure 2b), and the SPFH (Simplified PFH) features are obtained using statistical histograms. Weighted fusion of the SPFH features corresponding to the k nearest neighbor points is performed to obtain the FPFH features

$$FPFH(p_q) = SPFH(p_q) + \frac{1}{k}\sum_{i=1}^{k}\frac{1}{\omega_i}SPFH(p_{k_i}) \tag{3}$$

The influence of point pairs $\left\{p_{k_i}, p_{k_j}\right\}$ in the p_q neighborhood is approximated by $SPFH(p_{k_i})$, which facilitates parallel processing and improves computational efficiency. Also, as shown in Figure 2b, FPFH expands the neighborhood range (up to $2r$), which can enhance the feature characterization.

2.2. Matching Gross Rejection Based on Structural Features

Establishing feature descriptions based on the spatial structure between key points enables the coupling of global information, addressing the issue of mismatching caused by local feature similarity. In scenarios where the proportion of feature mismatches is high or the number of matches is limited, methods resembling RASANC [31,32] tend to converge to local optima, making it challenging to achieve robust estimation of registration relationships [33,34]. In recent years, graphs have seen widespread application in various research domains, including feature matching [35], image or point cloud segmentation [36,37], and object recognition [38,39]. Therefore, we employed a structure matching method incorporating high-dimensional spatial correlation to mitigate incorrect local feature matches. This method can be formulated as a graph matching problem, which can be mathematically described as:

$$\begin{gathered} \max_{\mathbf{X}} vec(\mathbf{X})^T \mathbf{K} vec(\mathbf{X}) \\ s.t. \mathbf{X} \in \{0,1\}^{N_1 \times N_2}, \mathbf{X}\mathbf{1}_{N_2} = \mathbf{1}_{N_1},\ \mathbf{X}^T\mathbf{1}_{N_1} \le \mathbf{1}_{N_2} \end{gathered} \tag{4}$$

where $\mathbf{X}$ is the assignment matrix and $\mathbf{K}$ is the affinity matrix, whose diagonal elements represent the first-order node similarity information and non-diagonal elements represent the second-order edge similarity information [40,41].

The purpose of graph matching is to compute the optimal assignment matrix $\mathbf{X}^*$ by optimizing the above objective function, which is an NP-hard problem [42]. However, since the matching relationship between point clouds can be adequately described by a 3D rigid-body transformation with shape and scale invariance, there is no need to consider higher-order correlations between nodes. By focusing solely on feature similarity (i.e., node similarity) and the similarity of edges formed by pairs of nodes, it becomes possible to effectively reduce the search space and enhance the efficiency of graph matching algorithms.

In order to simplify the graph matching problem and improve the computational efficiency, as shown in Figure 4, we constructed an association graph $\mathbf{K}$ corresponding to the graph matching problem based on the key point pairs $M = \{p_i q_i, i = 1, \ldots, N\}$ obtained by feature matching. Each node x_i in the graph represents a strategy (i.e., matching M_i), reflecting the feature similarity between key points, and each edge represents the correlation between different strategies M_i and M_j $(i \neq j)$, reflecting the second-order similarity corresponding to the spatial relationship. Since local feature matching has already filtered out most of the incorrect edges (i.e., mismatches), as well as nodes not involved in matching, the size of the graph is substantially smaller compared to traditional graph matching methods. This reduction in size is crucial for addressing the NP-hard problem within polynomial time. Polynomial time refers to a complexity class where the

time required to solve a problem increases polynomially, rather than exponentially, with the size of the input, making the solution computationally feasible for larger datasets. By leveraging this approach, the graph matching problem can be transformed into a graph-based gross error rejection problem.

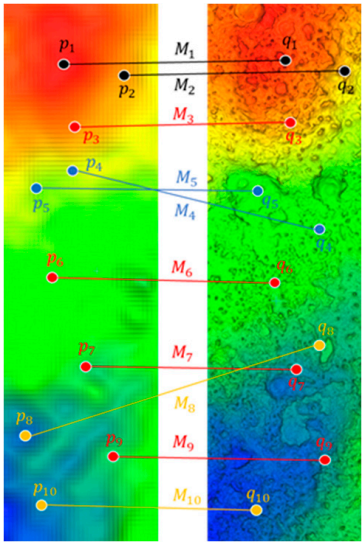

(**a**) Key point feature matching results

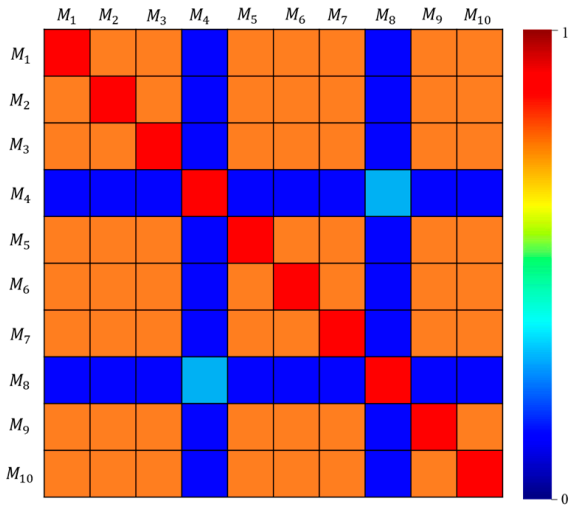

(**b**) Association graph **K**

Figure 4. Construction of graph matching problem. Here, (**a**) shows the results of key point matching, M_4 and M_8 indicate gross mismatches. (**a**) Left image is the MOLA DEM, and the right image is the HiRISE DEM. Elevation is represented through color rendering, with red indicating higher elevations and blue indicating lower elevations. And (**b**) is the association graph corresponding to (**a**).

Let the initial state N sets of matches $M_i(i = 1, \ldots, N)$ have the same confidence level and equal weights as $\frac{1}{N}$, i.e., $x_i = \frac{1}{N}$. On the basis of the distance similarity C_{dist} [43], the normal vector angle constraint C_{angle} is introduced, and then the correlation $\mathbf{K_{ij}}$ between match i and match j can be defined as

$$\begin{aligned} C_{dist}(i,j) &= e^{-(\|p_i - p_j\|_2 - \|q_i - q_j\|_2)^2} \\ C_{angle}(i,j) &= e^{-(|cos<p_i - p_j, n_{p_i}>| - |cos<q_i - q_j, n_{q_i}>|)^2} \\ \mathbf{K_{ij}} &= \tfrac{1}{2} \times \Big(C_{dist}(i,j) + C_{angle}(i,j) \Big) \end{aligned} \tag{5}$$

It should be noted that C_{angle} can reduce the influence of nearby points of optimal matching on the results and improve the robustness of the algorithm to resolution differences.

In the optimization process, the overall gain $\mathrm{G}(\mathbf{x}, \mathbf{K})$ is maximized by adjusting the weight vector $\mathbf{x}$ and reallocating the confidence degree of each node, similar to the non-cooperative game problem solving process. The matching game's objective function is defined as

$$(\mathbf{x}, \mathbf{K}) = \mathbf{x}^{\mathbf{T}} \mathbf{K} \mathbf{x} \; s.t. \forall i, x_i > 0, \sum_{i=1}^{N} x_i = 1 \tag{6}$$

$$\hat{\mathbf{x}} = \underset{\mathbf{x}}{\mathrm{argmax}} \mathrm{G}(\mathbf{x}, \mathbf{K}) \; s.t. \forall i, x_i \geq 0, \sum_{i=1}^{N} x_i = 1 \tag{7}$$

The graph matching problem is further transformed into a conditional extremal problem under inequality constraints as in (11). It can be solved by the Lagrange multiplier

method under the KKT [44] condition. The Lagrangian function of the matching game function under the inequality constraint is defined as

$$L(\mathbf{x}, \boldsymbol{\mu}, \lambda) = \mathrm{G}(\mathbf{x}, \mathbf{K}) + \lambda \left(1 - \sum_{i=1}^{N} x_i \right) + \boldsymbol{\mu} \cdot \mathbf{x} \tag{8}$$

where $\mathrm{G}(\mathbf{x}, \mathbf{K})$ is the game objective function, $\lambda \left(1 - \sum_{i=1}^{N} x_i \right)$ is the equation constraint, and $\boldsymbol{\mu} \cdot \mathbf{x}$ is the inequality constraint. The corresponding KKT conditions are

$$\begin{array}{c} \frac{\partial L}{\partial \mathrm{x}} = 0 \\ \lambda \neq 0,\ \mu_i \geq 0,\ \mu_i x_i = 0 \\ 1 - \sum_{i=1}^{N} x_i = 0, x_i \geq 0 \end{array} \tag{9}$$

Referring to the numerical approach for non-cooperative games [45], the system of KKT conditional equations above is solved iteratively to obtain the weight vector $\hat{\mathbf{x}}$ corresponding to maximum overall gain $\mathrm{G}(\mathbf{x}, \mathbf{K})$.

$$x_i(t) = x_i(t-1) \frac{\sum_{j=1}^{N} K_{i,j} \cdot x_j(t-1)}{\sum_{i=1}^{N} \sum_{j=1}^{N} K_{i,j} \cdot x_i(t-1) x_j(t-1)},\ i = 1, \ldots, N \tag{10}$$

where t denotes the t-th iteration and $x_i(0) = \frac{1}{N}$.

Since the goal of coarse registration is to calculate the coarse alignment matrix based on a small number of good quality matches, we rearranged the weight vectors $\hat{\mathbf{x}}$ obtained from the solution in descending order, taking the top 10% matches as good quality matches, and obtaining the coarse alignment matrix by least squares estimation.

3. DEM Fine Registration Based on Improved VGICP

The coarse registration algorithm serves as an effective solution to the point cloud registration problem, particularly when the relative positions are entirely unknown. However, the registration process is affected by the distribution and density of key points, and considering only a limited number of key point pairs makes it challenging to achieve precise local alignment. Since the goal of terrain matching is to attain the absolute orientation of the reconstructed Digital Elevation Model (DEM), performing local fine registration becomes essential.

Building upon feature coarse registration, accurate correspondence between point clouds is achieved by minimizing the point-to-point distance metric function. The classical Iterative Closest Point (ICP) algorithm [24] determines the optimal transformation between point clouds by minimizing the distance from each source point to its nearest neighbor in the target point cloud, enabling point-to-point registration. However, this method is sensitive to gross errors and resolution disparities. In contrast, the point-to-plane ICP [46] minimizes the distance from each source point to the plane where the corresponding target point is located, leveraging spatial information from the neighborhood of the target point for point-to-distribution registration. This approach exhibits faster convergence and greater resistance to gross errors compared to traditional ICP, but it does not consider the local information of the source point, making it challenging to handle mismatches caused by gross errors in the source point cloud. The Generalized Iterative Closest Point (GICP) algorithm [47] addresses these limitations by weighting the distance loss based on both the local geometric information of the source and target points, achieving distribution-to-distribution alignment. GICP outperforms both point-to-point ICP and point-to-plane ICP in terms of registration accuracy and robustness. Another approach, the Normal Distributions Transform (NDT) algorithm [48], voxelizes the target point cloud before matching and determines the optimal transformation by maximizing the response value of the probability function corresponding to the projection of the source points onto the target voxel distribution. NDT operates as a voxel-based point-to-distribution method. However,

NDT is often highly sensitive to the choice of voxel resolution, and its registration accuracy tends to be lower than that of ICP methods. The geometric interpretation of the distance cost associated with these methods is illustrated in Figure 5.

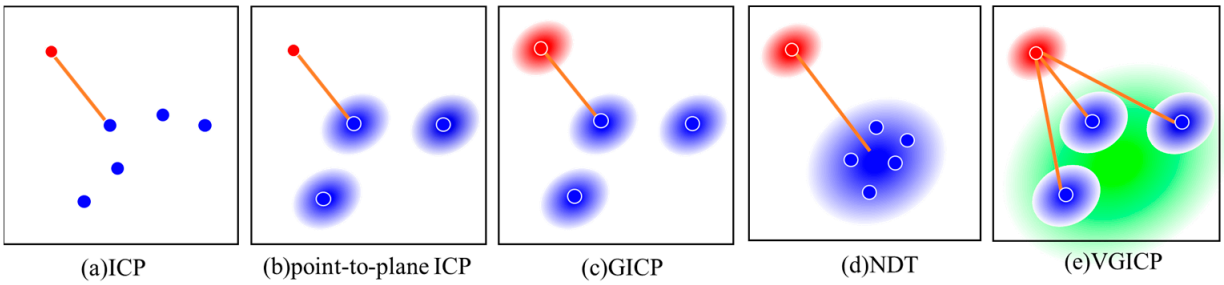

Figure 5. Geometric illustration of distance cost [49].

The Voxelized Generalized Iterative Closest Point (VGICP) [49] algorithm borrows the concept of voxels, considers the relationship between the source point distribution and all distributions within the nearest neighboring voxels, and weights the inter-distribution loss by the number of points within the voxel grid to achieve distribution-to-multi-distribution smoothness matching, which can improve the GICP algorithm in terms of both running speed and robustness. VGICP simultaneously calculates the distance between the source point $\boldsymbol{a}_i \sim N\left(\hat{\boldsymbol{a}}_i, \boldsymbol{C}_i^A\right)$ to multiple target points $\boldsymbol{b}_j \sim N\left(\hat{\boldsymbol{b}}_j, \boldsymbol{C}_j^B\right)$ in a neighborhood of radius r. The cumulative sum $\hat{\boldsymbol{d}}_i'$ is taken as a single point loss

$$\hat{\boldsymbol{d}}_i' = \sum_j (\hat{\boldsymbol{b}}_j - \mathbf{T}\hat{\boldsymbol{a}}_i) \tag{11}$$

By considering multiple local distributions, the local features can be smoothed effectively. Assuming that $\boldsymbol{a}_i$ and $\boldsymbol{b}_j$ are independent of each other, it follows that

$$\boldsymbol{d}_i' \sim N\left(\sum_j (\hat{\boldsymbol{b}}_j - \mathbf{T}\hat{\boldsymbol{a}}_i), \sum_j \left(\boldsymbol{C}_j^B + \mathbf{T}\boldsymbol{C}_i^A\mathbf{T}^T\right)\right) = N\left(0, \sum_j \left(\boldsymbol{C}_j^B + \mathbf{T}\boldsymbol{C}_i^A\mathbf{T}^T\right)\right) \tag{12}$$

Converting the solution process of the registration matrix $\mathbf{T}$ to a maximum likelihood problem as

$$\mathbf{T}^* = \underset{\mathbf{T}}{argmin} \sum_i \left(\sum_j (\hat{\boldsymbol{b}}_j - \mathbf{T}\hat{\boldsymbol{a}}_i)\right)^T \left(\sum_j \left(\boldsymbol{C}_j^B + \mathbf{T}\boldsymbol{C}_i^A\mathbf{T}^T\right)\right)^{-1} \left(\sum_j (\hat{\boldsymbol{b}}_j - \mathbf{T}\hat{\boldsymbol{a}}_i)\right) \tag{13}$$

$$\mathbf{T}^* = \underset{\mathbf{T}}{argmin} \sum_i N_i \left(\frac{\sum_j \hat{\boldsymbol{b}}_j}{N_i} - \mathbf{T}\hat{\boldsymbol{a}}_i\right)^T \left(\frac{\sum_j \boldsymbol{C}_j^B}{N_i} + \mathbf{T}\boldsymbol{C}_i^A\mathbf{T}^T\right)^{-1} \left(\frac{\sum_j \hat{\boldsymbol{b}}_j}{N_i} - \mathbf{T}\hat{\boldsymbol{a}}_i\right) \tag{14}$$

where N_i is the number of points in the neighborhood (i.e., within the voxel).

VGICP takes into account local smoothing, which is robust against local area differences resulted from point cloud sampling granularity and source data resolution, and thus better solves the MOLA DEM and HiRISE DEM registration problems. However, similar to NDT, the voxel radius r has a large impact on the registration accuracy. In order to reduce the sensitivity of voxel radius r selection, we improved VGICP by smoothing and weighting the loss and covariance terms in (18) using the Euclidean distance from $\boldsymbol{a}_i$ to $\boldsymbol{b}_j$, so that the weights of different points within the voxel are different (as in Figure 6). The maximum likelihood problem of our improved method can be described as

$$\mathbf{T}^* = \underset{\mathbf{T}}{argmin} \sum_i \left\{ \left(\sum_j \omega_{ij} \right) \left(\frac{\sum_j \omega_{ij} \hat{\boldsymbol{b}}_j}{\sum_j \omega_{ij}} - \mathbf{T}\hat{\boldsymbol{a}}_i \right)^T \left(\frac{\sum_j \omega_{ij} \boldsymbol{C}_j^B}{\sum_j \omega_{ij}} + \mathbf{T}\boldsymbol{C}_i^A\mathbf{T}^T \right)^{-1} \left(\frac{\sum_j \omega_{ij} \hat{\boldsymbol{b}}_j}{\sum_j \omega_{ij}} - \mathbf{T}\hat{\boldsymbol{a}}_i \right) \right\} \tag{15}$$

$$\omega_{ij} = exp\left(-\frac{\left\| \hat{\boldsymbol{b}}_j - T\hat{\boldsymbol{a}}_i \right\|^2}{2\sigma^2} \right) \tag{16}$$

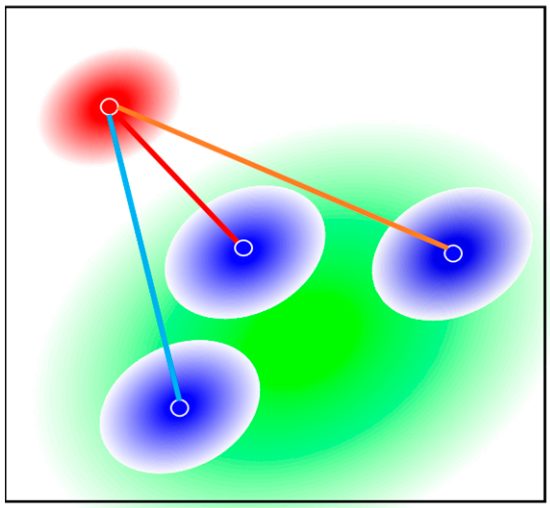

Figure 6. Distance cost of our method (lines with different colors represent different weights).

However, since the calculation process of ω_{ij} involves $\mathbf{T}$, the iterative process needs to constantly repeat the calculation of $\frac{\sum_j \omega_{ij} \hat{\boldsymbol{b}}_j}{\sum_j \omega_{ij}}$ and $\frac{\sum_j \omega_{ij} \boldsymbol{C}_j^B}{\sum_j \omega_{ij}}$. To improve the computational efficiency, we approximate $\mathbf{T}\hat{\boldsymbol{a}}_i$ by the geometric center $\overline{\boldsymbol{b}}_i^r$ of the points $\boldsymbol{b}_j$ inside the voxel, then the expression ω_{ij} after the approximate substitution is defined as

$$\omega_{ij} = exp\left(-\frac{\left\| \hat{\boldsymbol{b}}_j - \overline{\boldsymbol{b}}_i^r \right\|^2}{2\sigma^2} \right) \tag{17}$$

where $\overline{\boldsymbol{b}}_i^r = \frac{\sum_j \hat{\boldsymbol{b}}_j}{N_i}$, σ is the width parameter of the Gaussian kernel function.

4. Experiment and Analysis

4.1. Experimental Data

In order to verify the effectiveness of the proposed method, topographic data for the proposed Curiosity landing area, Mawrth Vallis, were selected for the experiments. Mawrth Vallis is located in the Oxia Palus quadrangle, sitting approximately two kilometers below the Martian datum. It is a channel that was formed by massive ancient floods on Mars. Orbital data have revealed the presence of hydrated minerals and abundant deposits of light-colored clays in the Mawrth Vallis region, indicating that it was once submerged in a water environment. Clays are excellent at preserving biosignatures, making this region an ideal target for studying the history of life on Mars. Additionally, its location between the southern highlands and the northern lowlands offers a relatively flat terrain, making it more suitable for rover landings.

The experimental data include Mars Orbiting Laser Altimeter (MOLA) DEM and HiRISE DEM. MOLA DEM is a digital elevation model covering the globe of Mars based on MOLA data carried by NASA MGS, with a horizontal positioning accuracy of 100 m,

an elevation accuracy of 3 m, and a pixel resolution of 463 m. Global MOLA DEM images use a simple cylindrical projection with a size of 23,040 × 46,080 pixels (Figure 7a). In this paper, the target point cloud was generated by resampling the DEM images within the study area (longitude 19.15°W~18.94°W, latitude 23.74°N~24.19°N), and the sampling resolution was 16 m in order to ensure the point cloud order of magnitude was consistent with HiRISE DEM (as in Figure 7b).

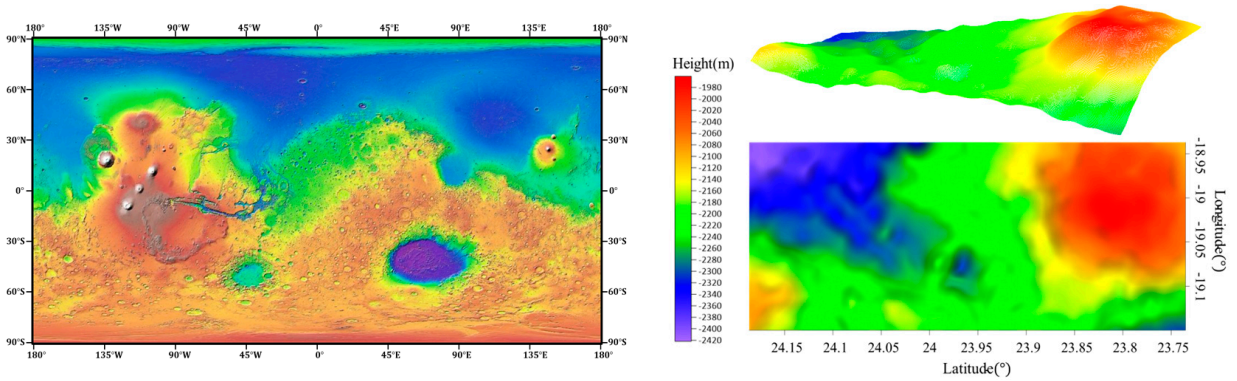

(**a**) (**b**)

Figure 7. MOLA experimental data. (**a**) Global MOLA DEM image; (**b**) MOLA sampling result.

The HiRISE DEM was generated by the Mars orbit image photogrammetry processing software developed by our team. This software was developed in the C + + language and has functions such as line-array image intensive matching, jitter correction, bundle block adjustment, etc. The generated DEM achieves a sub-pixel accuracy in terms of back projection error. The HiRISE stereo image pairs are PSP_008469_2040 and PSP_008825_2040 from the Mawrth Vallis area (Figure 8a) with a ground resolution of 0.25 m. Due to the large amount of data, the experiments in this paper use a uniform grid of 64 × 64 pixels to extract the thinning and perform a semi dense surface reconstruction to obtain the HiRISE DEM grid with 16 m resolution (as in Figure 8b).

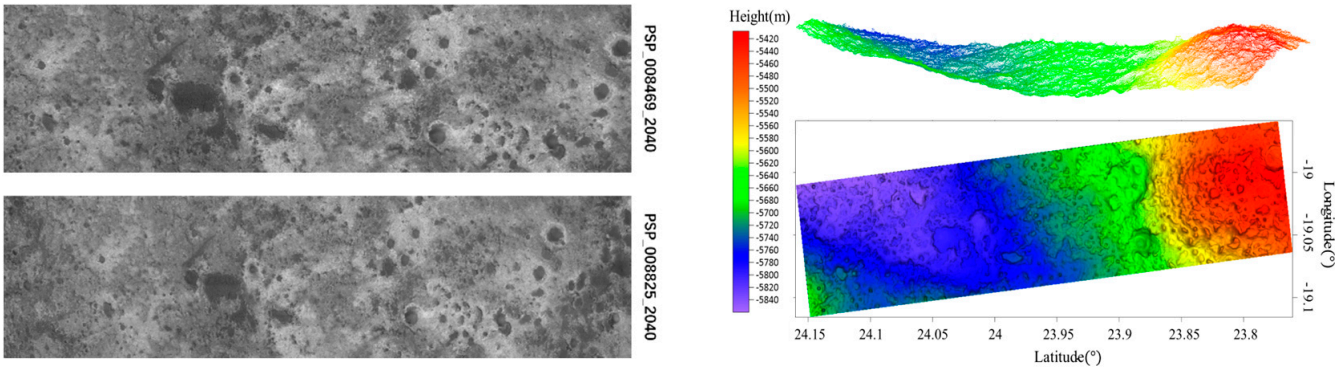

(**a**) (**b**)

Figure 8. HiRISE Experimental data. (**a**) HiRISE stereo image; (**b**) HiRISE DTM.

Comparing Figures 7b and 8b, it is easy to see that the sampling area of MOLA DEM is relatively larger, the topographic resolution of HiRISE DEM is much higher than that of MOLA DEM, and the difference in local details between the two is huge, while the average elevation difference between the two is greater than 3000 m.

4.2. Evaluation Metrics

Common point cloud registration evaluation metrics include L2 Norm Loss (Squared Error), Root Mean Square Error (RMSE), Largest Common Point Set (LCP), Chamfer

Distance (CD), and so on. Due to the large difference in the detail resolution between the HiRISE DEM and the MOLA DEM, we used the statistical mean value of point pair errors m_i in the local area as the unit loss, and we took the sum by inverse variance weighting as the global registration error of the terrain. The algorithm is as follows:

1. Calculate the k nearest neighbors $\boldsymbol{b}_{jl}(l = 1, \ldots, k)$ in the target point cloud for point $\boldsymbol{a}_j$ in the source point cloud, and calculate their mean $\hat{\boldsymbol{b}}_j$ as a virtual nearest neighbor.

$$\hat{\boldsymbol{b}}_j = \frac{\sum_{l=1}^{k} \boldsymbol{b}_{jl}}{k} \tag{18}$$

2. Block the registration area with a homogeneous grid and calculate the mean and variance of the registration coordinate differences of the point pairs within the grid.

$$\begin{aligned} m_i &= \frac{\sum_{\boldsymbol{a}_j \in A_i, \boldsymbol{b}_j \in B_i} \left\| \hat{\boldsymbol{b}}_j - \mathbf{T}\boldsymbol{a}_j \right\|}{N_i} \\ \sigma_i^2 &= \frac{\sum_{\boldsymbol{a}_j \in A_i, \boldsymbol{b}_j \in B_i} \left(\left\| \hat{\boldsymbol{b}}_j - \mathbf{T}\boldsymbol{a}_j \right\| - m_i \right)^2}{N_i} \end{aligned} \tag{19}$$

3. Weight the mean value of the registration coordinate differences m_i for all grids using the inverse variance $\frac{1}{\sigma_i^2}$ and then calculate the mean value as the terrain registration error δ_{TM}:

$$\delta_{TM} = \sum_{i=0}^{N_{bs}} \frac{m_i}{\sigma_i^2} / \sum_{i=0}^{N_{bs}} \frac{1}{\sigma_i^2} \tag{20}$$

where N_{bs} is the number of grids.

In addition, the RMSE, LCP, and CD metrics can be defined as

$$\begin{aligned} \text{RMSE} &= \sqrt{\frac{\sum_{i=0}^{N} \|\boldsymbol{b}_i - \mathbf{T}\boldsymbol{a}_i\|^2}{N}} \\ \text{LCP} &= count\{a_i | \|\boldsymbol{b}_i - \mathbf{T}\boldsymbol{a}_i\| < \epsilon, \boldsymbol{a}_i \in A, \boldsymbol{b}_i \in B\} \\ \text{CD} &= \frac{1}{N_1} \sum_{\boldsymbol{a}_i \in A} \min_{\boldsymbol{b}_j \in B} \|\boldsymbol{b}_i - \mathbf{T}\boldsymbol{a}_i\| + \frac{1}{N_2} \sum_{\boldsymbol{b}_j \in B} \min_{\boldsymbol{a}_i \in A} \left\|\boldsymbol{b}_j - \mathbf{T}\boldsymbol{a}_i\right\| \end{aligned} \tag{21}$$

4.3. Coarse Registration Results

Before terrain coarse registration, we generated the point cloud grid corresponding to HiRISE and MOLA terrain data with 16 m spacing using the reconstruction and resampling methods. According to the method in Section 2, ISS key point extraction and key point FPFH feature descriptions are performed first, then nearest neighbor matching is performed to obtain the initial correspondence of key points, and reliably matched point pairs are obtained after graph matching to reject gross errors.

The number of experimental point clouds, ISS feature point extraction results and matching results are shown in Table 1.

Table 1. Coarse registration results.

	Number Points	ISS Key Points	Initial Matching	Graph Match Optimization
MOLA	349,674	2409	1336	136
HiRISE	143,774	3639		

Although the number of sampling points for the MOLA DEM is much larger than that for the HiRISE DEM, the number of ISS key points is less instead because of its lower initial resolution and the relatively gentle elevation undulation between sampling points. As shown in Figure 9a, there are a large number of mismatches among the 1336 pairs of initial matches obtained by the feature space nearest neighbor search. We performed the mismatch rejection using the structural feature method proposed in Section 2.2 and obtained 136 pairs of high-quality correspondences (as in Figure 9b). From the visual

perspective, a large number of matching gross errors were eliminated and the remaining matches had a good spatial consistency.

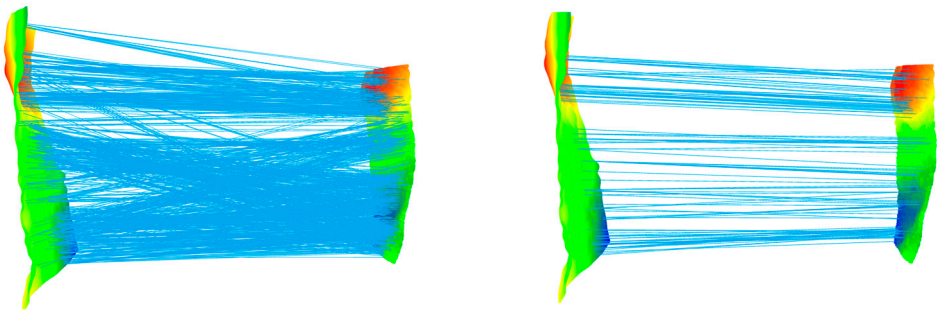

(**a**) (**b**)

Figure 9. Key points matching results. (**a**) FPFH feature matching; (**b**) optimization based on graph matching. The initial feature matching contains numerous mismatches (**a**), but after applying graph matching to remove gross errors, the remaining matches are correct (**b**).

The results of the coarse registration are shown in Figure 10. The black line in Figure 10a is caused by elevation differences, reflecting the fact that the accuracy of the coarse registration is still limited, as is the difference in elevation of the elliptically labelled area in Figure 10b and the uneven occlusion in Figure 10c (ideally, the greyscale MOLA DEMs should be uniformly distributed with the color HiRISE DEMs).

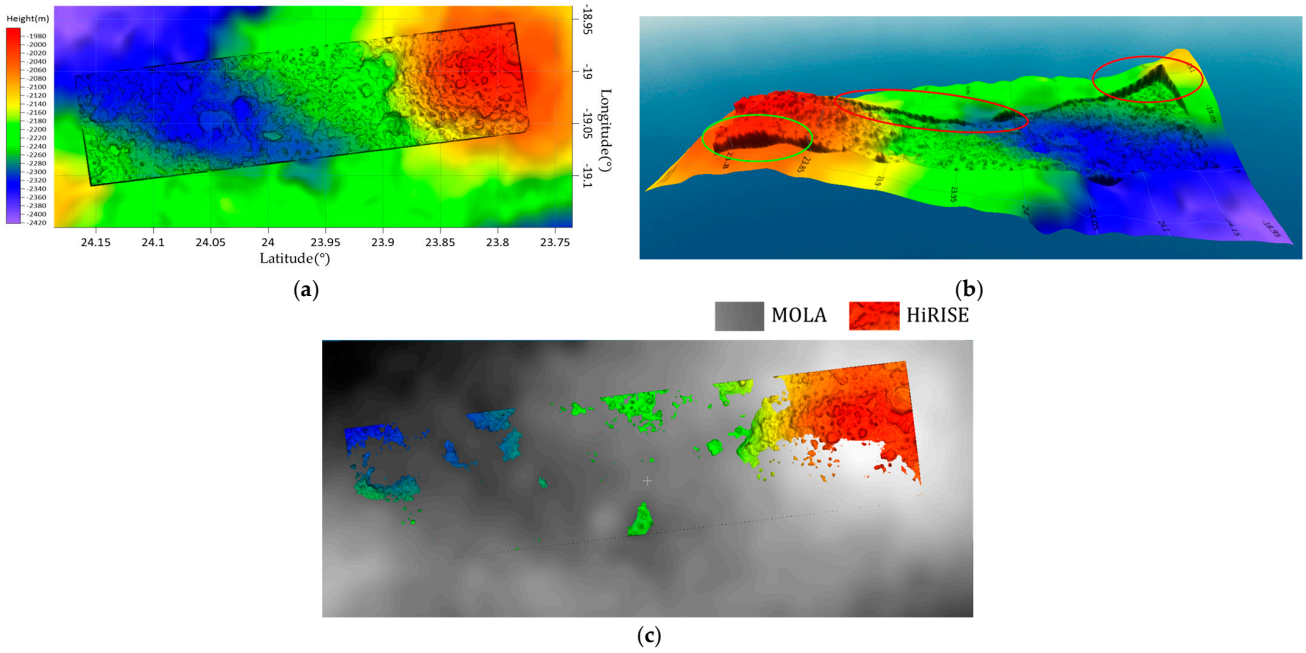

(**a**) (**b**)

(**c**)

Figure 10. Coarse registration results. (**a**) Coarse registration mapping; (**b**) 3D views of registration result; (**c**) Top view of point cloud registration. The black dots, lines, and boundaries in (**a**) represent elevation discrepancies at the edges of DEM registration, and the ellipses in (**b**) highlight areas with significant elevation differences.

From Figures 7b and 8b, it can be seen that, before the alignment, the average elevation in the HiRISE DEM was −5600 m, while in the MOLA DEM it was −2200 m. After coarse registration, the average elevation difference was reduced from >3000 m to about 101 m, and the overall terrain fits with MOLA DEM. Therefore, the coarse registration algorithm can realize the rough positioning of HiRISE DEM in the global range. However, as shown in Figure 10b, there are still some areas with poor registration, resulting in clear differences

in elevation at the junction. The accuracy evaluation indexes of the coarse registration algorithm are shown in Table 2.

Table 2. Coarse registration precision.

Algorithm	δ_{TM}/m	RMSE/m	LCP	CD/m
ISS + FPFH	101.261	143.276	623	675.100

4.4. Fine Registration Results

The coarse registration achieves geometric localization on a global scale. The coarse registration result can be used as the initial registration state to further realize point-by-point registration based on the improved VGICP and to compare it with the classical ICP, GICP, and VGICP methods. In the experiment, in order to eliminate the local mismatch caused by the difference in the original resolution of the HiRISE DEM and MOLA DEM, and verify the terrain registration capability of the algorithm based on sparse point clouds, the source and target point clouds were sampled sparsely with the same resolution; the down-sampled grid size was taken as V_s = 400 m, which is similar to the original resolution of the MOLA DEM. The upper limit for the algorithm iterations was set to 50. During the algorithm iterations, we evaluated the accuracy using checkpoints selected from the original point cloud (16 m resolution). The variation in the RMSE metrics of the four algorithms with the number of iterations is shown in Figure 11.

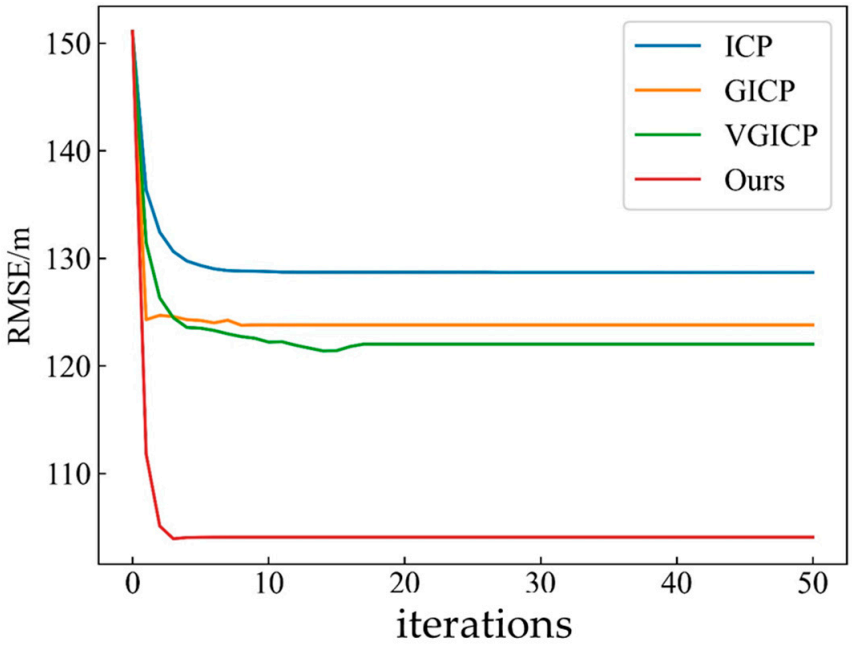

Figure 11. Comparison of algorithm convergence performance.

A visualization of the mean value of the coordinate differences within the grid when the iterations converge is shown in Figure 12 (corresponding to δ_{TM}). The accuracy statistics are shown in Table 3.

Table 3. Fine registration precision.

Algorithm	δ_{TM}/m	RMSE/m	LCP	CD/m
ICP	97.226	128.760	709	664.771
GICP	93.273	123.804	757	630.082
VGICP	91.836	122.014	770	642.532
Ours	**79.072**	**104.068**	**830**	**620.426**

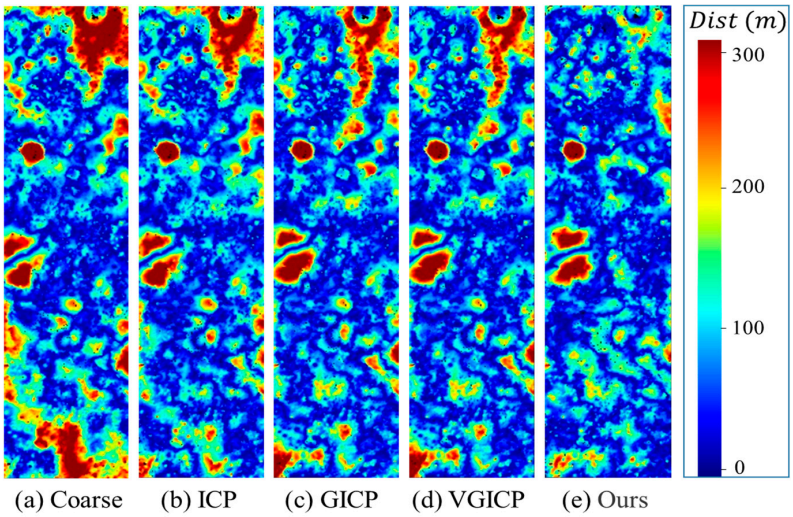

Figure 12. Visualization of the mean spatial registration error m_i within the grids using Equation (19). Uneven spatial errors are caused by the difference in spatial resolution between the MOLA DEM and HiRISE DEM.

By comparing the accuracy metrics in Tables 2 and 3, it can be seen that all four of the above fine registration algorithms can improve the coarse registration results, which is consistent with the results in Figure 12. At the same time, the performance of our method was better than the other three comparison algorithms in all of the evaluation indexes, and the mean value of the statistical pointing error of the grid δ_{TM} was reduced to below 80 m, and the number of LCP common points with MOLA DTM also significantly increased. As shown in Figure 10, compared with the existing best-performing VGICP algorithm, our algorithm converges faster and the RMSE is reduced by nearly 20%, which can achieve a high accuracy and high efficiency of HiRISE DEM absolute positioning. The final top view of the point cloud registration is shown in Figure 13. In terms of visual effects, the pixel ratios of the MOLA DEM and HiRISE DEM are the most similar in the top view corresponding to our method, and the distribution is more random, which means that the terrain fits better and the inconsistency of the registration results reflects the difference in the resolution ability of the terrain itself more rather than the gross errors in the registration.

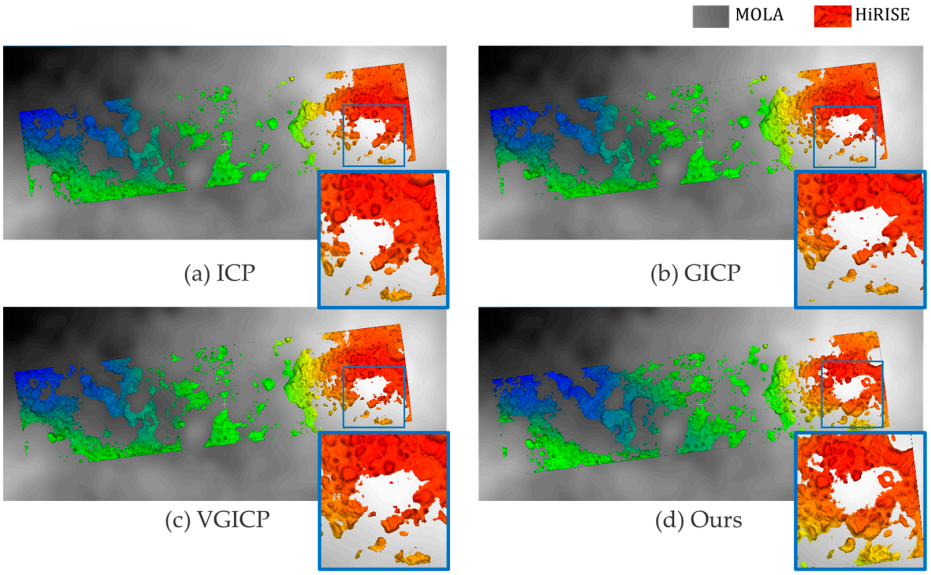

Figure 13. Top view of fine registration results. The performance of the realignment can be judged from the degree of mosaicking of the HiRISE DEM and the MOLA DEM. More uniformity indicates better alignment results.

Meanwhile, in order to verify the stability of the selection of voxel radius r, a comparison experiment with VGICP was designed by taking $r = \{V_s, 2V_s, \ldots, 5V_s\}$, and the number of iterations as 50. The variation in the RMSE index with the number of iterations is shown in Figure 14, and the statistical results are shown in Table 4.

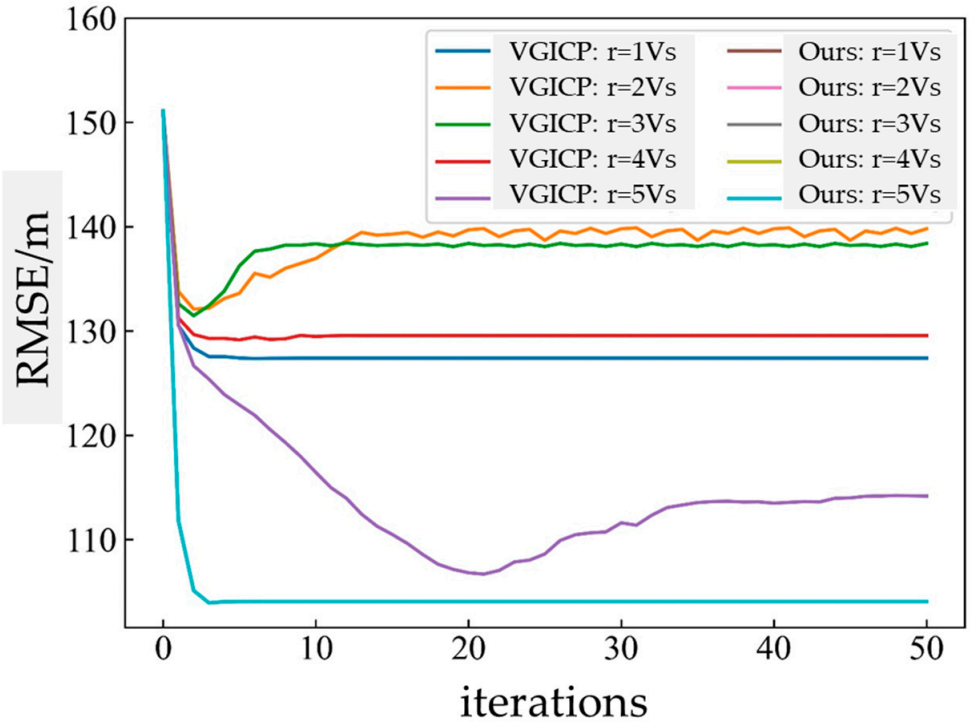

Figure 14. Influence of voxel radius r. The overlapping lines of our method indicate that the results are almost identical, demonstrating our method remains best performance when different voxel radius r is chosen.

Table 4. Influence of voxel radius r.

Algorithm	r (V_s = 400 m)	RMSE/m
VGICP	V_s	127.38818962202778
	$2V_s$	139.79158193437294
	$3V_s$	138.31933973779917
	$4V_s$	129.55025475600053
	$5V_s$	111.60038788194028
Ours	V_s	104.06773202236396
	$2V_s$	104.06773202298623
	$3V_s$	104.06773202298623
	$4V_s$	104.06773202298623
	$5V_s$	104.06773202298623

Analyzing the experimental results, it can be seen that, when $r = V_s, 2V_s, \ldots, 5V_s$, the RMSE difference corresponding to the smoothing weighting method used in this paper is less than 10^{-9} m. Therefore, the method in this paper is not sensitive to the selection of the voxel radius r, which can avoid the influence of r on the fine registration results and effectively improves the robustness of the algorithm.

The fine registration mapping results are shown in Figure 15.

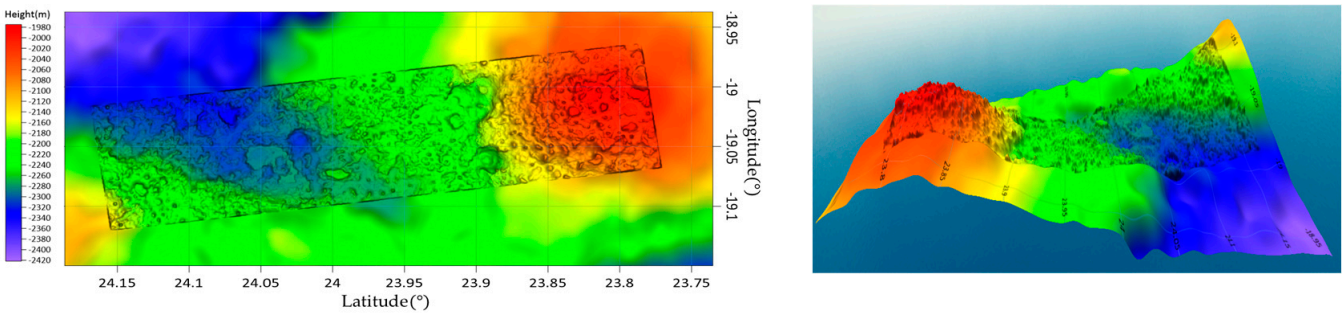

(**a**) (**b**)

Figure 15. Fine registration results. (**a**) Registration mapping; (**b**) 3D visualization.

5. Conclusions

In this paper, a DEM coarse registration framework based on the combination of ISS + FPFH features was proposed to obtain the initial feature correspondence between different terrain data according to a feature description of key points and nearest neighbor matching in the feature space, and to reject the feature matching gross errors by introducing the strategy of graph matching, which finally achieves the global coarse localization of HiRISE DEM. In the process of fine registration, in order to solve the problem of large difference in detail resolution between MOLA DEM and HiRISE DEM, we modified the VGICP method by smoothly weighting the loss and covariance through the Euclidean distance between distributions, which improved the robustness of the algorithm. Experiments show that the proposed algorithm has the highest registration accuracy in the HiRISE DEM orientation task by comparing it with classical ICP, GICP, and VGICP algorithms. The method in this paper is adapted to multi-source terrain matching problems with large differences in detail resolution.

In future work, we plan to further explore the application of this method to positioning problems involving various Martian DEM data such as Tianwen-1 High Resolution Imaging Camera (HiRIC), HiRISE, and MOLA. Additionally, we aim to investigate direct registration methods between orbital imagery and DEMs, such as employing deep learning techniques to correlate features between images and point clouds to enhance the algorithm's stability. To counteract resolution differences, we are also considering studying error-adaptive weighted registration methods.

Author Contributions: Conceptualization, S.Z. and B.W.; methodology, B.W.; software, B.W.; validation, B.W. and X.G.; formal analysis, B.W. and X.G.; investigation, B.W.; resources, B.W.; data curation, B.W.; writing—original draft preparation, S.Z., B.W. and G.Y.; writing—review and editing, S.Z. and B.W.; visualization, B.W.; supervision, S.Z.; project administration, B.W.; funding acquisition, S.Z. All authors have read and agreed to the published version of the manuscript.

Funding: This research was funded by the China Major Project of High Resolution Earth Observation System (Civil Part), Project approval number: 06-Y30F04-9001-20/22.

Data Availability Statement: Data will be made publicly accessible at https://github.com/wbl1997/3D_DEM_registration (accessed on 28 April 2024).

Conflicts of Interest: The authors declare no conflicts of interest.

References

1. Qing, X.U.; Xun, G.; Chaozhen, L.A.N.; Shuai, X. Review of Mars Topographic Mapping. *J. Deep Space Explor.* **2014**, *1*, 28–35.
2. McEwen, A.S.; Eliason, E.M.; Bergstrom, J.W.; Bridges, N.T.; Hansen, C.J.; Delamere, W.A.; Grant, J.A.; Gulick, V.C.; Herkenhoff, K.E.; Keszthelyi, L. Mars Reconnaissance Orbiter's High Resolution Imaging Science Experiment (HiRISE). *J. Geophys. Res. Planets* **2007**, *112*. [CrossRef]
3. Rosiek, M.R.; Kirk, R.L.; Archinal, B.A.; Howington-Kraus, E.; Hare, T.; Galuszka, D.; Redding, B. Utility of Viking Orbiter Images and Products for Mars Mapping. *Photogramm. Eng. Remote Sens.* **2005**, *71*, 1187–1195. [CrossRef]

4. Kirk, R.L.; Howington-Kraus, E.; Redding, B.; Galuszka, D.; Hare, T.M.; Archinal, B.A.; Soderblom, L.A.; Barrett, J.M. High-resolution Topomapping of Candidate MER Landing Sites with Mars Orbiter Camera Narrow-angle Images. *J. Geophys. Res. Planets* **2003**, *108*. [CrossRef]
5. Kirk, R.; Soderblom, L.; Howington-Kraus, E.; Archinal, B.; Team, A. USGS High Resolution Topo-Mapping of Mars with Mars Orbiter Camera Narrow-Angle Images. *Int. Arch. Photogramm. Remote Sens. Spat. Inf. Sci.* **2002**, *34*, 713–722.
6. Shan, J.; Yoon, J.; Lee, D.S.; Kirk, R.L.; Neumann, G.A.; Acton, C.H. Photogrammetric Analysis of the Mars Global Surveyor Mapping Data. *Photogramm. Eng. Remote Sens.* **2005**, *71*, 97–108. [CrossRef]
7. Albertz, J.; Attwenger, M.; Barrett, J.; Casley, S.; Dorninger, P.; Dorrer, E.; Ebner, H.; Gehrke, S.; Giese, B.; Gwinner, K. HRSC on Mars Express–Photogrammetric and Cartographic Research. *Photogramm. Eng. Remote Sens.* **2005**, *71*, 1153–1166. [CrossRef]
8. Smith, D.E.; Zuber, M.T.; Frey, H.V.; Garvin, J.B.; Head, J.W.; Muhleman, D.O.; Pettengill, G.H.; Phillips, R.J.; Solomon, S.C.; Zwally, H.J. Mars Orbiter Laser Altimeter: Experiment Summary after the First Year of Global Mapping of Mars. *J. Geophys. Res. Planets* **2001**, *106*, 23689–23722. [CrossRef]
9. Abshire, J.B.; Sun, X.; Afzal, R.S. Mars Orbiter Laser Altimeter: Receiver Model and Performance Analysis. *Appl. Opt.* **2000**, *39*, 2449–2460. [CrossRef]
10. Li, R.; Hwangbo, J.; Chen, Y.; Di, K. Rigorous Photogrammetric Processing of HiRISE Stereo Imagery for Mars Topographic Mapping. *IEEE Trans. Geosci. Remote Sens.* **2011**, *49*, 2558–2572.
11. Wang, K.; Zhu, T.; Gao, Y.; Wang, J. Efficient Terrain Matching with 3-D Zernike Moments. *IEEE Trans. Aerosp. Electron. Syst.* **2018**, *55*, 226–235. [CrossRef]
12. Yoo, J.-C.; Han, T.H. Fast Normalized Cross-Correlation. *Circuits Syst. Signal Process.* **2009**, *28*, 819–843. [CrossRef]
13. Heidler, K.; Mou, L.; Baumhoer, C.; Dietz, A.; Zhu, X.X. HED-UNet: Combined Segmentation and Edge Detection for Monitoring the Antarctic Coastline. *IEEE Trans. Geosci. Remote Sens.* **2021**, *60*, 4300514. [CrossRef]
14. Sipiran, I.; Bustos, B. Harris 3D: A Robust Extension of the Harris Operator for Interest Point Detection on 3D Meshes. *Vis. Comput.* **2011**, *27*, 963–976. [CrossRef]
15. Scovanner, P.; Ali, S.; Shah, M. A 3-Dimensional Sift Descriptor and Its Application to Action Recognition. In Proceedings of the 15th ACM International Conference on Multimedia, Augsburg, Germany, 25–29 September 2007; pp. 357–360.
16. Chen, H.; Bhanu, B. 3D Free-Form Object Recognition in Range Images Using Local Surface Patches. *Pattern Recognit. Lett.* **2007**, *28*, 1252–1262. [CrossRef]
17. Zaharescu, A.; Boyer, E.; Varanasi, K.; Horaud, R. Surface Feature Detection and Description with Applications to Mesh Matching. In Proceedings of the 2009 IEEE Conference on Computer Vision and Pattern Recognition, Miami, FL, USA, 20–25 June 2009; pp. 373–380.
18. Zhong, Y. Intrinsic Shape Signatures: A Shape Descriptor for 3D Object Recognition. In Proceedings of the 2009 IEEE 12th International Conference on Computer Vision Workshops, ICCV Workshops, Kyoto, Japan, 24 September–27 October 2009; pp. 689–696.
19. Salti, S.; Tombari, F.; Di Stefano, L. SHOT: Unique Signatures of Histograms for Surface and Texture Description. *Comput. Vis. Image Underst.* **2014**, *125*, 251–264. [CrossRef]
20. Rusu, R.B.; Marton, Z.C.; Blodow, N.; Beetz, M. Persistent Point Feature Histograms for 3D Point Clouds. In Proceedings of the 10th International Conference on Intelligent Autonomous Systems (IAS-10), Baden-Baden, Germany, 23–25 July 2008; pp. 119–128.
21. Rusu, R.B.; Blodow, N.; Beetz, M. Fast Point Feature Histograms (FPFH) for 3D Registration. In Proceedings of the 2009 IEEE International Conference On Robotics and Automation, Kobe, Japan, 12–17 May 2009; pp. 3212–3217.
22. Gojcic, Z.; Zhou, C.; Wegner, J.D.; Wieser, A. The Perfect Match: 3d Point Cloud Matching with Smoothed Densities. In Proceedings of the IEEE/CVF Conference on Computer Vision and Pattern Recognition, Long Beach, CA, USA, 15–20 June 2019; pp. 5545–5554.
23. Rosenholm, D.A.N.; TORLEGARD, K. Three-Dimensional Absolute Orientation of Stereo Models Using Digital Elevation Models. *Photogramm. Eng. Remote Sens.* **1988**, *54*, 1385–1389.
24. Besl, P.J.; McKay, N.D. Method for Registration of 3-D Shapes. In *Sensor Fusion IV: Control Paradigms and Data Structures*; SPIE: Bellingham, WA, USA, 1992; Volume 1611, pp. 586–606.
25. Chen, X.; Cen, M.; Guo, H.; Zhang, T.; Zhao, C.; Zhang, B. Chinese Satellite Photogrammetry without Ground Control Points Based on a Public DEM Using an Efficient and Robust DEM Matching Method. *Int. J. Remote Sens.* **2018**, *39*, 704–726. [CrossRef]
26. Arvidson, R.E.; Bell III, J.F.; Bellutta, P.; Cabrol, N.A.; Catalano, J.G.; Cohen, J.; Crumpler, L.S.; Des Marais, D.J.; Estlin, T.A.; Farrand, W.H. Spirit Mars Rover Mission: Overview and Selected Results from the Northern Home Plate Winter Haven to the Side of Scamander Crater. *J. Geophys. Res. Planets* **2010**, *115*. [CrossRef]
27. Welch, R.; Limonadi, D.; Manning, R. Systems Engineering the Curiosity Rover: A Retrospective. In Proceedings of the 2013 8th International Conference on System of Systems Engineering, Maui, HI, USA, 2–6 June 2013; pp. 70–75.
28. Hwangbo, J.; Chen, Y.; Li, R. Precision processing of hirise stereo orbital images for topograpic mapping on mars. In Proceedings of the ASPRS 2010 Annual Conference, San Diego, CA, USA, 26–30 April 2010.
29. MOLA Team. Mars MGS MOLA DEM 463m V2. Available online: https://astrogeology.usgs.gov/search/map/Mars/GlobalSurveyor/MOLA/Mars_MGS_MOLA_DEM_mosaic_global_463m (accessed on 17 April 2024).
30. Zhou, R.; Li, X.; Jiang, W. 3D Surface Matching by a Voxel-Based Buffer-Weighted Binary Descriptor. *IEEE Access* **2019**, *7*, 86635–86650. [CrossRef]

31. Torr, P.H.; Zisserman, A. MLESAC: A New Robust Estimator with Application to Estimating Image Geometry. *Comput. Vis. Image Underst.* **2000**, *78*, 138–156. [CrossRef]
32. Tordoff, B.J.; Murray, D.W. Guided-MLESAC: Faster Image Transform Estimation by Using Matching Priors. *IEEE Trans. Pattern Anal. Mach. Intell.* **2005**, *27*, 1523–1535. [CrossRef]
33. Lebeda, K.; Matas, J.; Chum, O. Fixing the Locally Optimized Ransac–Full Experimental Evaluation. In *British Machine Vision Conference*; Citeseer: Princeton, NJ, USA, 2012; Volume 2.
34. Li, J.; Hu, Q.; Ai, M. LAM: Locality Affine-Invariant Feature Matching. *ISPRS J. Photogramm. Remote Sens.* **2019**, *154*, 28–40. [CrossRef]
35. Cho, M.; Lee, J.; Lee, K.M. Reweighted Random Walks for Graph Matching. In Proceedings of the Computer Vision–ECCV 2010: 11th European Conference on Computer Vision, Heraklion, Crete, Greece, 5–11 September 2010; Proceedings, Part V 11. Springer: Berlin/Heidelberg, Germany, 2010; pp. 492–505.
36. Elibol, A.; Gracias, N.; Garcia, R.; Kim, J. Graph Theory Approach for Match Reduction in Image Mosaicing. *J. Opt. Soc. Am. A* **2014**, *31*, 773–782. [CrossRef] [PubMed]
37. Xu, Y.; Hoegner, L.; Tuttas, S.; Stilla, U. Voxel-and Graph-Based Point Cloud Segmentation of 3D Scenes Using Perceptual Grouping Laws. *ISPRS Ann. Photogramm. Remote Sens. Spat. Inf. Sci.* **2017**, *4*, 43–50. [CrossRef]
38. Berner, A.; Bokeloh, M.; Wand, M.; Schilling, A.; Seidel, H.-P. A Graph-Based Approach to Symmetry Detection. In Proceedings of the 7th International Symposium on Volume Graphics, 5th Symposium on Point-Based Graphics, VG/PBG@ SIGGRAPH, Los Angeles, CA, USA, 10–11 August 2008; pp. 1–8.
39. Wu, J.; Shen, H.; Li, Y.-D.; Xiao, Z.-B.; Lu, M.-Y.; Wang, C.-L. Learning a Hybrid Similarity Measure for Image Retrieval. *Pattern Recognit.* **2013**, *46*, 2927–2939. [CrossRef]
40. Umeyama, S. An Eigendecomposition Approach to Weighted Graph Matching Problems. *IEEE Trans. Pattern Anal. Mach. Intell.* **1988**, *10*, 695–703. [CrossRef]
41. Belongie, S.; Malik, J.; Puzicha, J. Shape Matching and Object Recognition Using Shape Contexts. *IEEE Trans. Pattern Anal. Mach. Intell.* **2002**, *24*, 509–522. [CrossRef]
42. Leordeanu, M.; Hebert, M. A Spectral Technique for Correspondence Problems Using Pairwise Constraints. In Proceedings of the Tenth IEEE International Conference on Computer Vision (ICCV'05) Volume 1, Washington, DC, USA, 17–20 October 2005; IEEE: Piscataway, NJ, USA, 2005; Volume 2, pp. 1482–1489.
43. Li, J.; Hu, Q.; Ai, M. GESAC: Robust Graph Enhanced Sample Consensus for Point Cloud Registration. *ISPRS J. Photogramm. Remote Sens.* **2020**, *167*, 363–374. [CrossRef]
44. Luenberger, D.G. *Introduction to Linear and Nonlinear Programming*; Addison-Wesley: Boston, MA, USA, 1973.
45. Hofbauer, J.; Sigmund, K. *Evolutionary Games and Population Dynamics*; Cambridge University Press: Cambridge, UK, 1998.
46. Chen, Y.; Medioni, G. Object Modelling by Registration of Multiple Range Images. *Image Vis. Comput.* **1992**, *10*, 145–155. [CrossRef]
47. Segal, A.; Haehnel, D.; Thrun, S. Generalized-Icp. In *Robotics: Science and Systems*; MIT Press: Seattle, WA, USA, 2009; Volume 2, p. 435.
48. Biber, P.; Straßer, W. The Normal Distributions Transform: A New Approach to Laser Scan Matching. In Proceedings of the 2003 IEEE/RSJ International Conference on Intelligent Robots and Systems (IROS 2003) (Cat. No. 03CH37453), Las Vegas, NV, USA, 27–31 October 2003; Volume 3, pp. 2743–2748.
49. Koide, K.; Yokozuka, M.; Oishi, S.; Banno, A. Voxelized Gicp for Fast and Accurate 3d Point Cloud Registration. In Proceedings of the 2021 IEEE International Conference on Robotics and Automation (ICRA), Xi'an, China, 30 May–5 June 2021; pp. 11054–11059.